Superior magnetic and mechanical property of MnFe_{3}N driven by electron correlation and lattice anharmonicity

Hao Wu, Hong Sun, and Changfeng Chen

Phys. Rev. B **91**, 064102 — Published 5 February 2015

DOI: 10.1103/PhysRevB.91.064102

Superior magnetic and mechanical property of $MnFe_3N$ driven by electron correlation and lattice anharmonicity

Hao Wu,[1] Hong Sun,[2,*] and Changfeng Chen[3,†]

[1]*Department of Physics and Astronomy and Key Laboratory of Artificial Structures and Quantum Control (Ministry of Education), Shanghai Jiao Tong University, Shanghai 200240, China*

[2]*Department of Physics and Astronomy and Key Laboratory of Artificial Structures and Quantum Control (Ministry of Education), Shanghai Jiao Tong University, Shanghai 200240, and Collaborative Innovation Center of Advanced Microstructures, Nanjing University, Nanjing 210093, China*

[3]*Department of Physics and High Pressure Science and Engineering Center, University of Nevada, Las Vegas, Nevada 89154, USA*

(Dated: January 20, 2015)

Abstract

Manganese substitution doped iron nitride $MnFe_3N$ holds great promise for applications in high-density magnetic recording and spintronic devices. However, existing theory contradicts experimental results on the structural and magnetic stability of $MnFe_3N$, and the underlying mechanisms remain elusive. Here we demonstrate by first-principles calculations that the ferromagnetic state with enhanced magnetization in $MnFe_3N$ is driven by the electron correlation effect not previously considered. We further reveal a large nonlinear shear plasticity, which produces an unexpectedly high shear strength in $MnFe_3N$ despite its initial ductile nature near the equilibrium structure. Moreover, we identify strong lattice anharmonicity that plays a pivotal role in stabilizing $MnFe_3N$ under high pressures at the room temperature. These remarkable properties stem from the intriguing bonding nature of the parent compound Fe_4N. Our results explain experimental results and offer insights into the fundamental mechanisms for the superior magnetic and mechanical property of $MnFe_3N$.

PACS numbers: 75.50.-y,62.20.-x,81.40.Jj,63.20.-e

I. INTRODUCTION

Iron nitride Fe_4N (γ'-phase) produced in nitriding process is widely used to improve the wear, fatigue and corrosion resistance of iron and steel surfaces[1–4]. In recent years, Fe_4N also attracted great interest for its large saturation magnetization and high spin polarization ratio (SPR), which have been extensively studied experimentally[5–12] and theoretically[13–22] to explore potential applications in high-density magnetic recording and spintronic devices. High quality single phase (001) Fe_4N films have been grown by molecular beam epitaxy on various substrates[23–27]. While these concerted efforts have produced a wealth of knowledge about properties of Fe_4N and its derivative structures, these studies also have raised important questions about fundamental mechanisms underlying the observed phenomena. In particular, a number of key experimental results still lack a consistent theoretical explanation, and in some cases theory and experiment contradict each other. The following issues, among others, must be resolved to establish a sound understanding of the experimental results for further exploration of this class of materials for applications.

(i) Recent studies indicate that Mn substitution doping is possibly the only doping process that can further enhance the magnetic moment of Fe_4N, and this sets $MnFe_3N$ apart from other transitional-metal doped Fe_4N structures that show reduced magnetization[28–36]. The enhanced magnetism by Mn substitution is highly desirable for device applications, and it also offers an additional avenue to probe the fundamental physics governing the property of the Fe_4N class of materials. Previous density functional theory (DFT) calculations indicated that the $MnFe_3N$ structure with Mn substitution on the face-center position has the lowest total energy, and this structure has a reduced magnetization compared to that of Fe_4N[35]. This is in stark contrast to the result of recent Mössbauer and X-ray diffraction study that showed that Mn mainly occupies the cubic corner position in $MnFe_3N$[36], and such a structure possesses enhanced magnetization[35]. Such discrepancy between theory and experiment must be resolved to understand the fundamental mechanisms that determine the structural and magnetic property of $MnFe_3N$ that holds the key to successful applications.

(ii) Fe_4N exhibits enigmatic behavior in its elastic response, which requires a close examination of this fundamental mechanical property. The calculated ratio of its elastic constants C_{11}/C_{44} reaches a high value of about 300/50, which indicates a large bulk-to-shear-modulus ratio, thus a high ductility for Fe_4N[15]. It was even suggested that Fe_4N can be used as a

solid lubricant or damage tolerant ferromagnetic materials[31,33]. However, this contradicts the well-known fact that Fe_4N is the main structure obtained from nitriding processes, which can greatly improve the wear, fatigue and corrosion resistance of iron and steel surfaces[1–4]. A full understanding of the structural strength of Fe_4N and the influence by the Mn substitution doping in $MnFe_3N$ require a thorough study of the stress-strain relations of these materials under large deformation. In particular, we need to explore possible strain-stiffening[37] that may happen at large (shear) strains, which could lead to (shear) strength enhancement that cannot be predicted by elastic constants determined at the equilibrium structure. Determination of the full-range stress-strain relations of Fe_4N and $MnFe_3N$ from DFT calculations can provide a better understanding of their mechanical properties, such as tensile and shear strength and ductility.

(iii) Another important issue regarding Fe_4N and its derivative structures like $MnFe_3N$ concerns their structural stability at high pressures. X-ray diffraction experiments revealed that Fe_4N structure persists under pressure up to 30 GPa at the room temperature, though new phases appear and coexist at lower pressures[7,8,10,12]. Our calculations, however, show that in the harmonic approximation soft phonon modes appear in Fe_4N and $MnFe_3N$ at pressures much lower than 30 GPa, indicating dynamical instability in their structures. It is necessary to examine the effect of lattice anharmonicity on structural stability by finite-temperature phonon calculations[38]. Such results would establish key benchmarks for structural stability and transformation in these materials.

In this paper, we report on a DFT study of Fe_4N and $MnFe_3N$. We first resolve the structural determination of $MnFe_3N$. Previous DFT calculations show that Mn prefers to substitute Fe atom at the face-center position of Fe_4N, resulting in a ferrimagnetic ground state of $MnFe_3N$[35]. This is in contrast to the recent experimental observation that Mn mainly substitutes Fe atom at the cubic corner position of Fe_4N[36], which will give rise to a ferromagnetic ground state of $MnFe_3N$ with enhanced magnetization. The reported DFT calculations used ordinary local density approximation (LDA) and generalized gradient approximation (GGA) for the exchange-correlation potentials[35]. However, a GGA+U scheme must be used in order to predict the correct structures for some Mn–N compounds. For instance, the experimentally observed rocksalt structure of MnN can only be predicted with a GGA+U (with U−J=2.9 eV for Mn) calculation, while ordinary GGA (or LDA) without the addition of the U term gives a zinc-blende structure for MnN[39]. The GGA+U scheme

TABLE I: Calculated lattice constant (a) in Å, bulk (B) and shear (G) modulus, and elastic constants (C_{ij}) in GPa, and Poisson's ratio (ν) for ferromagnetic Fe_4N and Mn^cFe_3N, which are compared to available experimental and other calculated data.

Ferromagnetic Fe_4N						
a	C_{11}	C_{12}	C_{44}	B	G	ν
3.802	308.5	136.5	45.4	194.3	57.6	0.365
3.790[a]				196[b]		
3.798[c]				155[d]		
3.795	307.2	134.1	46.0	191.8	59.4	0.360[e]
3.765	337	131	58.5	199.4	73.6	0.336[f]
Ferromagnetic Mn^cFe_3N						
a	C_{11}	C_{12}	C_{44}	B	G	ν
3.847	300.9	116.1	67.9	177.7	76.9	0.311

[a]Reference[5]
[b]Reference[6]
[c]Reference[7]
[d]Reference[8]
[e]Reference[15]
[f]Reference[33]

(with U−J=2.5 eV for Mn) was also used to study the structure and magnetic properties of $MnTi_2O_4$ under pressures[40]. In this work, we calculate the total energy of $MnFe_3N$ in different structures as functions of the U parameter of Mn (U_{Mn}). In the present GGA+U scheme, the parameters U and J always appear as a single term U−J, so we will drop explicit reference to parameter J in the following discussions. Our results show that as U_{Mn} increases to about 1 eV, the ferromagnetic state of $MnFe_3N$ with Mn occupying the cubic corner position has the lowest energy, which is consistent with the experimental results[36]. This indicates that the on-site Coulomb repulsion potentials, especially U_{Mn}, can stabilize more strongly the Mn d electron states when Mn occupies the cubic corner position in $MnFe_3N$, while in ordinary GGA calculations this effect is neglected. We next calculate from first-principles the stress-strain relations of Fe_4N and $MnFe_3N$, and determine the peak stresses (ideal strengths) under various deformation conditions. Such ideal strengths[41–51]

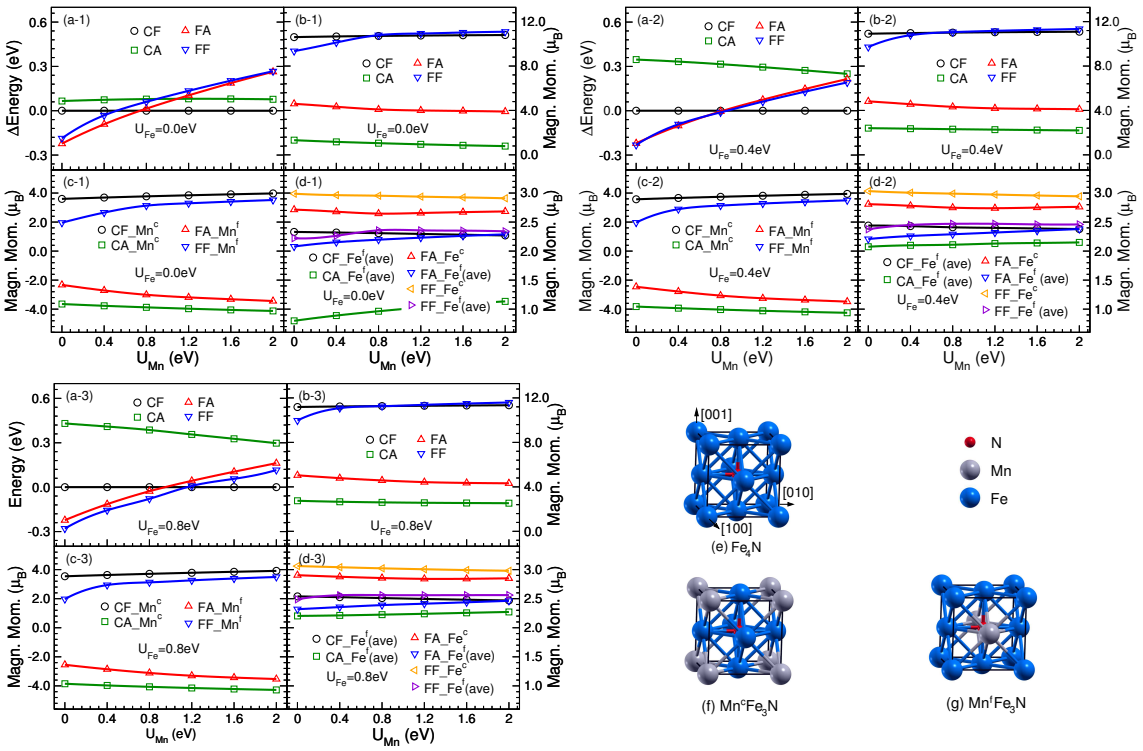

FIG. 1: (Color online) (a-i)(i=1,2,3) The calculated energy difference $\Delta E = E - E_{CF}$ for various $MnFe_3N$ structures as functions of the U parameter of Mn (U_{Mn}) with the U parameter of Fe (U_{Fe}) fixed at 0.0, 0.4 and 0.8 eV, where CF (CA) represents Mn occupying the cubic corner position of Fe_4N with ferromagnetic (anti-ferromagnetic) interactions between Mn and Fe; and FF (FA) represents Mn occupying the face center position of Fe_4N with ferromagnetic (anti-ferromagnetic) interactions between Mn and Fe. (b-i)(i=1,2,3) The calculated total (absolute) magnetic moments for various $MnFe_3N$ structures as functions of U_{Mn} with U_{Fe} fixed at 0.0, 0.4 and 0.8 eV. (c-i,d-i)(i=1,2,3) The calculated magnetic moment of Mn and Fe atoms for various $MnFe_3N$ structures as functions of U_{Mn} with U_{Fe} fixed at 0.0, 0.4 and 0.8 eV, where Mn^c (Mn^f) represents Mn occupying the cubic corner (face-center) position of Fe_4N, and Fe^c (Fe^f) represents Fe occupying the cubic corner (face-center) position of Fe_4N. The average values of the magnetic moments of Fe^f are plotted in (d-i)(i=1,2,3). (e-g) The unit cell of Fe_4N, $MnFe_3N$ with Mn occupying the cubic corner and face-center positions of Fe_4N.

determined for perfect crystals set an upper limit for material strengths, with ideal tensile strengths related to cleavage processes[42] and the ideal shear strengths to wear and hardness tests where well-controlled nano-indentation results could approach calculated ideal shear

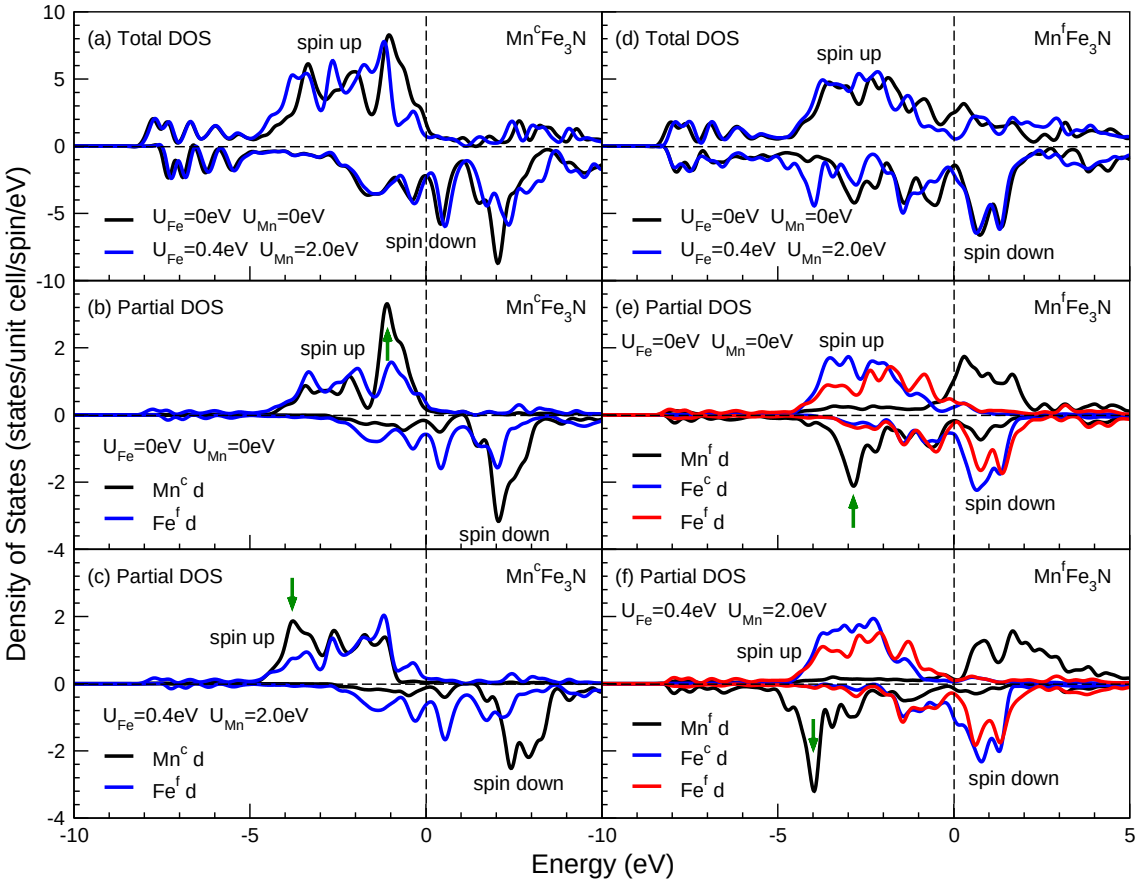

FIG. 2: (Color online) (a–c) The calculated total density of states (DOS) of the ferromagnetic Mn^cFe_3N with Mn occupying the cubic corner position and the partial DOS for its Mn atom at the cubic corner and the (three equivalent) Fe atoms at the face-center positions with U_{Fe}=0 eV; U_{Mn}=0 eV and U_{Fe}=0.4 eV; U_{Mn}=2.0 eV, respectively. (d–f) The calculated total DOS of the anti-ferromagnetic Mn^fFe_3N with Mn occupying the face-center position and the partial DOS for its Mn atom at the face-center, Fe atom at the cubic corner and the (two equivalent) Fe atoms at the face-center positions with U_{Fe}=0 eV; U_{Mn}=0 eV and U_{Fe}=0.4 eV; U_{Mn}=2.0 eV, respectively. The arrows in (b,c,e,f) indicate the distribution shifts of the electronic *d* states of Mn due to the on site repulsion potential U_{Mn}. The Fermi energy levels are set at the energy zeros.

strengths[49–51]. We report the calculated tensile and shear strengths of Fe_4N and $MnFe_3N$ on their (001), (011), (111) and (112) low index crystal planes. Our results show that both Fe_4N and $MnFe_3N$ have largest stiffness in the <001> directions, illustrated by the largest initial slopes of their [001] tensile stress-strain curves, but the tensile stress peaks in the [001] direction are still lower than those in the [111] direction. Among all the low index crystal

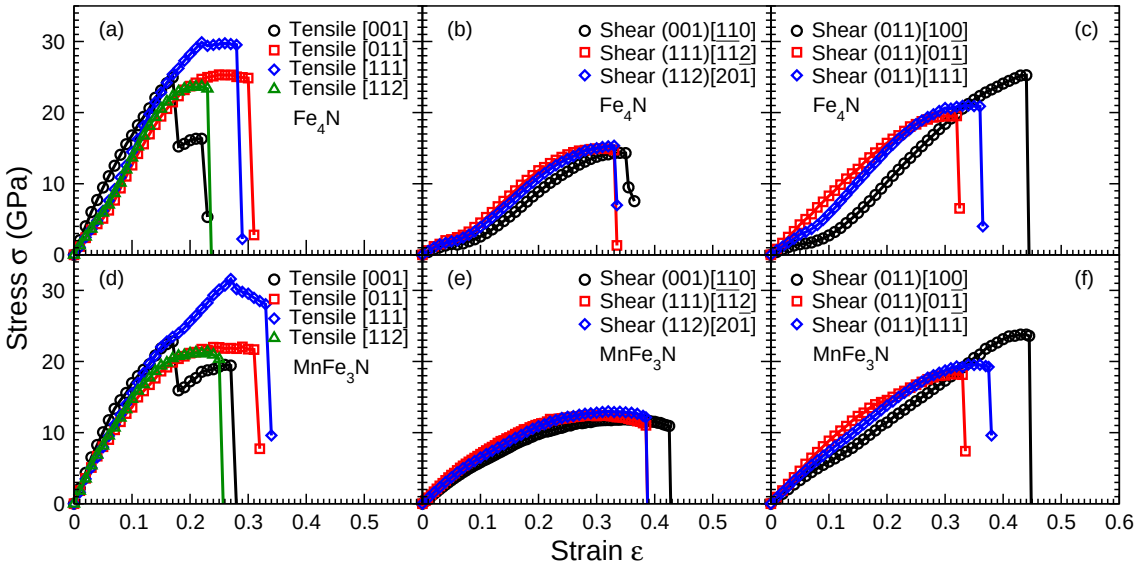

FIG. 3: (Color online) Calculated stress-strain relations for Fe_4N and $MnFe_3N$ (a,d) in tensile deformations, (b,e) in the weakest shear directions on the (001), (111) and (112) planes and (c,f) in all high symmetry shear directions on the (011) plane.

planes studied, the (011) plane has the strongest shear stress peaks (shear strengths) which are about 35% higher than those on all other planes, making the (011) plane the hardest and strongest wear resistance crystal plane of Fe_4N and $MnFe_3N$, much superior compared to other planes in mechanical properties. Our results also show that even though the ratio of the elastic constant $C_{11}/C_{44}\approx300/50$ is very large, which indicates a large ratio of the bulk to shear modulus (B/G) or possibly large ductility, the tensile strength (stress peaks) corresponding to the C_{11} deformation and shear strength (stress peak) corresponding to the C_{44} deformation at larger strains are about the same, with the shear strength increasing anomalously quickly (large nonlinear plasticity). This explains the fact that Fe_4N is the main layer structure in nitriding processes that can greatly improve the wear, fatigue and corrosion resistance of iron and steel surfaces[1–4]. Finally, we calculate the phonon spectra under pressure to study the dynamical stabilities of Fe_4N and $MnFe_3N$. The phonon spectra are first calculated with the harmonic approximation and then the phonon anharmonic interactions are considered at the room temperature (T=300K). Our results show that in the harmonic approximation, soft phonon modes appear in Fe_4N and $MnFe_3N$ under pressure at 14 GPa and 21 GPa, respectively. However, when the phonon anharmonic interactions are included, the soft phonon modes in Fe_4N and $MnFe_3N$ do not appear until pressure reaches

nearly 30 GPa at room temperature, which is consistent with the experimental observations. This large phonon anharmonicity is correlated with the large nonlinear shear plasticity.

II. CALCULATION METHODS

The DFT first-principles calculations of Fe_4N and $MnFe_3N$ were carried out using the VASP code[52], adopting the projector augmented wave (PAW) potentials[53] and generalized-gradient-approximation (GGA) for the exchange-correlation energy with a plane-wave basis set. The GGA-PBE exchange-correlation functional proposed by Perdew, Burke and Ernzerhof[54] was used, including the semi-core $3p$ electrons as the valence electrons for Fe and Mn. The total energy of the structure was minimized by relaxing the structural parameters using a conjugate gradient optimization method[55]. The total-energy and stress calculations were performed with a spin polarized configuration and used an initial cubic (or tetragonal) unit cell occupied by interstitial Mn atoms at various positions (see Fig. 1). A $9 \times 9 \times 9$ Monkhorst-Pack[56] k-point grid and a 500 eV energy cutoff were used in the calculations. The energy convergence of the calculation is on the order of 1 meV per atom, with the residual stresses and forces in the fully relaxed structures less than 0.1 GPa and 0.001 eV/Å. The quasistatic ideal strength and relaxed loading path were determined using a method described previously[41] in which the lattice vectors were incrementally deformed in the direction of the applied strains. At each step, the applied (tensile or shear) strain is fixed which determines the calculated (tensile or shear) stress, while the other five independent components of the strain tensors and all the atoms inside the unit cell were simultaneously relaxed until (i) all the residual components of the Hellmann-Feynman stress tensor orthogonal to the applied strain are less than 0.1 GPa, and (ii) the force on each atom becomes negligible ($<$0.001 eV/Å). The structure of the deformed unit cell is determined completely by this constrained atomic relaxation. The phonon spectra with the harmonic approximation and with the phonon anharmonic interactions at the room temperature (T=300K) were calculated using the PHONOPY[57] and SCAILD[58] codes with $2\times2\times2$ supercells for Fe_4N and $MnFe_3N$ under pressures. Test calculations were carried out for the equilibrium structures of Fe_4N and Mn^cFe_3N (ferromagnetic state with Mn at the cubic corner position of Fe_4N lattice) as well their elastic constants. The results are given in Table I, which agree well with the existing experimental and previously calculated results.

III. RESULTS AND DISCUSSIONS

Fig. 1(a-i)(i=1,2,3) shows the calculated total energy difference $\Delta E = E - E_{CF}$ for various $MnFe_3N$ structures as functions of the U parameter of Mn (U_{Mn}), and the U parameter of Fe (U_{Fe}) was fixed at 0.0, 0.4 and 0.8 eV following a recent work that tested various exchange-correlation functionals to interpret the structural, magnetic and hyperfine properties of Fe_4N and identified GGA-PBE+U with U=0.4 eV as the most accurate exchange-correlation functional for Fe in Fe_4N[18]. Also plotted in Fig. 1(b-i – d-i)(i=1,2,3) are the calculated total magnetic moments for various $MnFe_3N$ structures as functions of U_{Mn} and the calculated magnetic moment of Mn and Fe atoms for various $MnFe_3N$ structures as functions of U_{Mn} with U_{Fe} fixed at 0.0, 0.4 and 0.8 eV. The average values of the magnetic moments of Fe^f at the face-center positions are plotted in Fig. 1(d-i)(i=1,2,3). The results in Fig. 1(a-i)(i=1,2,3) clearly show that for all U_{Fe} used in the calculations the ferromagnetic Mn^cFe_3N structure with Mn at the cubic center positions has the lowest total energy when U_{Mn} is larger than 1.2 eV, which is consistent with the recent experimental finding that Mn mainly occupy the cubic corner positions in $MnFe_3N$[36]. Such a large U_{Mn} value in the GGA+U calculation was found to be necessary in MnN compound (with U−J=2.9 eV for Mn) to obtain the experimental observed rocksalt structure of MnN, while ordinary GGA (or LDA) with U_{Mn}=0 gives a zinc-blende structure for MnN[39]. The GGA+U calculation (with U−J=2.5 eV for Mn) was also adopted to study the structure and magnetic properties of $MnTi_2O_4$ under pressures[40]. The calculated magnetic moments of various $MnFe_3N$ structures in Fig. 1(b-i – d-i)(i=1,2,3) show that the results, especially the total magnetic moments, are insensitive to the change of U_{Mn} and U_{Fe}. The total magnetic moment of the ferromagnetic Mn^cFe_3N is about 11.1 μ_B, which is larger than that (10.3 μ_B) calculated for Fe_4N. The magnetization enhancement of the Mn^cFe_3N structure mainly comes from the large magnetic moment (3.94 μ_B) of Mn on the cubic corner position [see Fig. 1(c-i)(i=1,2,3)].

The on-site Coulomb repulsion potentials U_{Fe} and U_{Mn} have a significant impact on the electronic structures of $MnFe_3N$. We show in Fig. 2 the calculated total density of states (DOS) of the ferromagnetic Mn^cFe_3N with Mn occupying the cubic corner position and the partial DOS for its Mn atom at the cubic corner and the (three equivalent) Fe atoms at the face-center positions with U_{Fe}=0 eV; U_{Mn}=0 eV and U_{Fe}=0.4 eV; U_{Mn}=2.0 eV, respectively. Also shown are the calculated total DOS of the antiferromagnetic Mn^fFe_3N

with Mn occupying the face-center position and the partial DOS for its Mn atom at the face-center, Fe atom at the cubic corner and the (two equivalent) Fe atoms at the face-center positions with U_{Fe}=0 eV; U_{Mn}=0 eV and U_{Fe}=0.4 eV; U_{Mn}=2.0 eV, respectively. The general effect of the on-site repulsion, such as U_{Mn}, is to increase the splitting between the occupied spin up (down) and unoccupied spin down (up) states of the Mn electronic d orbital [see Fig. 2(b,c,e,f)]. When Mn is at the cubic corner, its d electrons are more localized inside the Mn atom comparing to those when Mn is at the face-center where strong covalent interactions between the N atom at the cubic-center and Mn atom at the face-center cause the delocalization of the electrons [see Fig. 1(f,g)]. So for the same U_{Mn}=2.0 eV, the energy splitting between the occupied spin and unoccupied (reversed) spin d states, or the energy shifting of the occupied spin d states towards lower energy level, is larger for the Mn at the cubic corner than that for the Mn at the face-center. The arrows in Fig. 2(b,c,e,f) indicate these energy shifts. This explains that as U_{Mn} increases, the total energy of Mn^cFe_3N eventually becomes lower than that of Mn^fFe_3N [see Fig. 1(a-i)(i=1,2,3)].

Another interesting effect of the on-site Coulomb repulsion is the enhancement of the SPR in Mn^cFe_3N. From Fig. 2(a) one finds that the total DOS at the Fermi energy (D_{E_F}) is reduced for the spin-up electrons as U_{Mn} increases, while that for the spin-down electrons keeps the same, so SPR=$(D^+_{E_F}-D^-_{E_F})/(D^+_{E_F}+D^-_{E_F})$ enhances from -0.11 with U_{Mn}=U_{Fe}=0 to -0.53 with U_{Mn}=2.0 eV and U_{Fe}=0.4 eV, which is comparable to the SPR (-0.66) of Fe_4N calculated with U_{Fe}=0.4 eV. Hereinafter, we limit our discussions only to the ferromagnetic Mn^cFe_3N structure [see Fig. 1(f)] and simplify its notation as $MnFe_3N$. All the remaining calculations are carried out with U_{Fe}=0.4 eV and U_{Mn}=2.0 eV.

We next examine the stress-strain relations of Fe_4N and $MnFe_3N$ in different tensile and shear loading directions. Previous calculations showed that the <001> direction is the stiffest direction in Fe_4N with the maximum Young's modulus produced by the strong covalent bonding between Fe atoms at the face-center and N atoms at the cubic-center positions, while all face-center cubic austenitic steel has the <111> direction as their stiffest direction[15]. Our results in Fig. 3 (a,d) show that the initial slopes of the stress-strain curves at small tensile strains in the [001] direction are indeed the largest for both Fe_4N and $MnFe_3N$; however, their tensile strengths (peak stresses) in the [001] direction are much lower than those in the [111] direction, which are the largest tensile strengths of Fe_4N and $MnFe_3N$. For the shear strength, we find that the (011) crystalline plane has much stronger

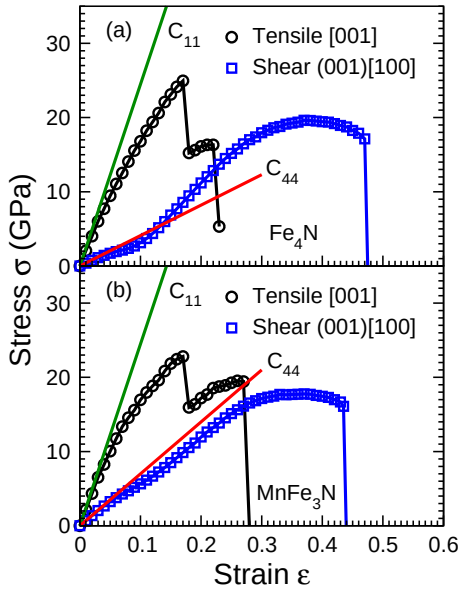

FIG. 4: (Color online) Calculated stress-strain relations for (a) Fe_4N and (b) $MnFe_3N$ in the [001] tensile direction and (001)[100] shear direction. The initial slopes of these curves equal the elastic constants of C_{11} and C_{44}.

shear strength than those on other low index planes. Fig. 3 (b,e) show the stress-strain relations in the weakest shear directions on the (001), (111) and (112) planes in Fe_4N and $MnFe_3N$, and Fig. 3 (c,f) show the stress-strain curves in all high symmetry shear directions on the (011) plane of Fe_4N and $MnFe_3N$. The shear strengths, which are the lowest peak stresses in various shear directions, in the (001), (111) and (112) planes in Fe_4N and $MnFe_3N$ are all about 15 GPa, while those in the (011) plane are about 20 GPa. These results indicate high scratching hardness and wear resistance in the (011) planes of Fe_4N and $MnFe_3N$.

The results of our present work (see Table I) and those form previous calculations[15,33] all show that Fe_4N exhibits a very large ratio of its bulk modulus B to its elastic constant C_{44}, $B/C_{44} = 3.4 \sim 4.2$, which indicates a high degree of ductility for Fe_4N. It was even suggested that Fe_4N and similar materials with large ratio of B/C_{44} can be used as solid lubricants or damage tolerant ferromagnetic materials[31,33]. However, this assessment is in contrast to the fact that Fe_4N forms the main surface layer structure in nitriding processes that can greatly improve the wear, fatigue and corrosion resistance of iron and steel surfaces[1–4]. To solve this paradox, we analyze the elastic constants of Fe_4N and $MnFe_3N$, which are determined by the initial stress response near the equilibrium structures, and compare them with their tensile and shear strengths (i.e., stress peaks), which occur at large deformation strains

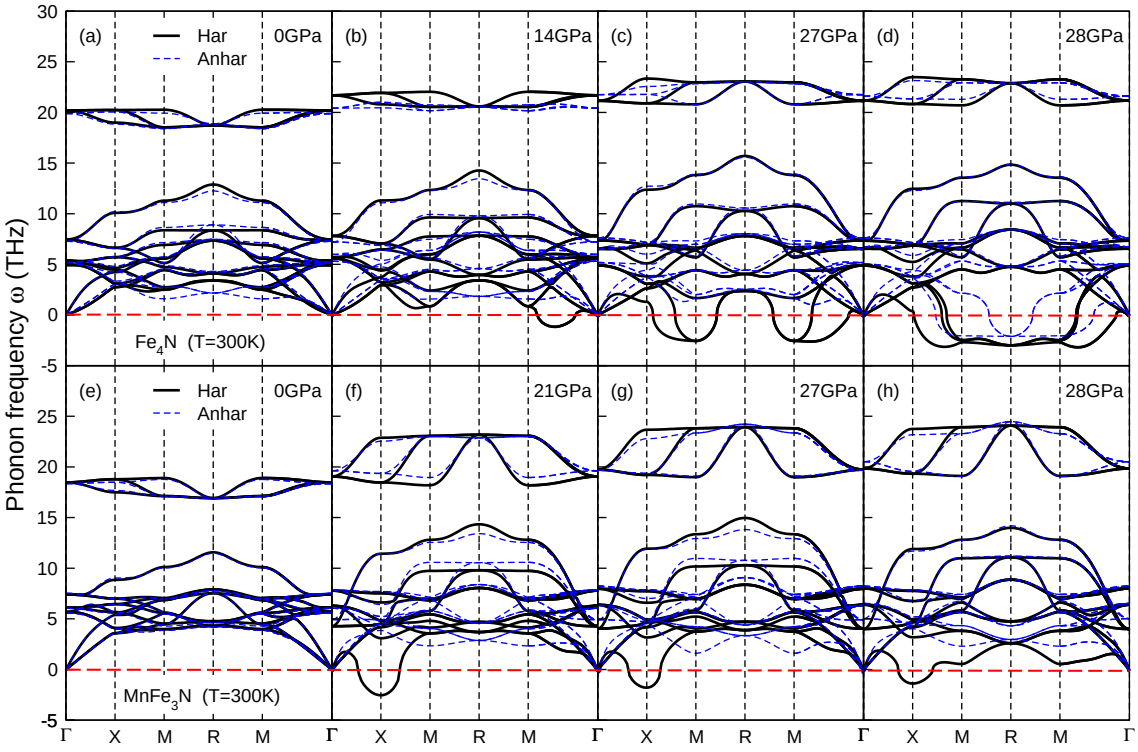

FIG. 5: (Color online) Calculated phonon spectra of (a–d) Fe_4N and (e–h) $MnFe_3N$ under different pressures with the harmonic approximation (the solid curves) and with phonon anharmonic interactions (the dashed curves) at T=300K. Imaginary phonon frequencies are given as negative frequencies.

along various crystalline directions. For a cubic structure like Fe_4N, its bulk modulus is given by $B = (C_{11} + C_{12})/3 \approx C_{11}/2$, where we approximate $C_{12} \approx C_{11}/2$ (see Table I). So $B/C_{44} \approx \frac{1}{2}C_{11}/C_{44}$. In Fig. 4 we plot the stress-strain curves under the [001] tensile and (001)[100] shear deformation directions for Fe_4N and $MnFe_3N$, where the initial slopes of these two curves equal the elastic constants C_{11} and C_{44}, respectively. The results in Fig. 4 (a) show that the initial slope in the (001)[100] shear stress-strain curve is low, which indicates a soft stress response, thus resulting in a large ratio of C_{11}/C_{44}. But the shear stress in the (001)[100] direction rises quickly with rising shear strains. Such a strong nonlinear plasticity effect is highly unusual in crystalline solids, which is similar to the strain-stiffening effect recently discovered in Fe_3C where the shear (010)[001] stress-strain curve has an initially soft stress response, but the shear stress increases quickly at large shear strains due to the rebonding of the atoms that reenforces the lattice structure[37]. This nonlinear strain stiffening behavior is observed in many shear stress-strain curves of Fe_4N

and $MnFe_3N$ (see Fig. 3 and Fig. 4). Such strong nonlinear plasticity may be correlated with other mechanical anomalies of the materials, such as the phonon anharmonic interactions, which can affect the dynamical instability (soft phonon modes) of the materials at finite temperature[38].

To probe the lattice anharmonicity in Fe_4N and $MnFe_3N$, we have calculated their phonon spectra at room temperature (T=300K) under pressure. Two sets of results were obtained, one under the harmonic approximation and the other with the phonon anharmonic interactions included[38]. The results calculated under the harmonic approximation [Fig. 4 (a–d)] show that dynamical instability appears in Fe_4N as pressure reaches 14 GPa as soft phonon modes start to develop. These soft phonon modes, however, are lifted once the phonon anharmonic interactions are turned on and, consequently, the structure of Fe_4N remains dynamically stable until the pressure reaches 28 GPa at T=300K. This result is consistent with the experimental X-ray diffraction observations, which indicate that the Fe_4N phase persists to a pressure range around 30 GPa[7,8,12]. This structural stabilization at a moderate temperature (T=300K) indicates a strong lattice anharmonicity in Fe_4N. It should be noted, however, that at low temperatures (T$\sim$0K) the phonon vibration amplitudes are small and the anharmonic lattice interactions will become weak. In that case, the phonon spectra should be well described by the harmonic approximation, which means that the structure of Fe_4N will become dynamically unstable at the lower pressure of about 14 GPa. The pressure dependence of the phonon spectra of $MnFe_3N$ shows a similar pattern; but under the harmonic approximation, $MnFe_3N$ becomes dynamically unstable when the pressure is higher than 21 GPa. This result indicates that Mn substitution has strengthened the lattice stability and delayed the onset of the soft phonon modes. With the inclusion of the anharmonic interactions at room temperature (T=300K), the $MnFe_3N$ structure remains dynamically stable at 28 GPa, which further demonstrates the role of substitution doped Mn in stabilizing the srystal structure.

IV. CONCLUSIONS

In summary, we have shown by first-principles GGA+U calculations that Mn substitution doping produces a ferromagnetic ground state of $MnFe_3N$ with the Mn atoms replacing Fe atoms at the cubic corner positions. This is because the on-site Coulomb repulsion

potentials, especially U_{Mn}, can stabilize more strongly the Mn d electron states when Mn occupies the cubic corner position in $MnFe_3N$, while in ordinary GGA calculations this effect is neglected. Our calculation explains recent experimental observations that in Mn-doped Fe_4N Mn atoms mainly substitute the cubic-corner Fe atoms. The resulting $MnFe_3N$ phase exhibits enhanced magnetization that is important to its device applications. Our first-principles stress-strain calculations show that, although Fe_4N exhibits the largest Young's modulus along the [001] direction, its largest tensile strength occurs in the [111] direction; the same phenomenon is observed in $MnFe_3N$. Moreover, both Fe_4N and $MnFe_3N$ have the largest shear strength of about 20 GPa in their (011) plane, which is 35% higher than those in all of their other sliding planes. This large shear strength is achieved by a remarkable nonlinear stress response that undergoes a steep rise at large strains, a phenomenon highly unusual for a crystalline solid. Our results suggest that the (011) planes of Fe_4N and $MnFe_3N$ possess the highest scratching hardness and wear resistance, which make them suitable for applications in high density magnetic recording heads and other applications. In particular, it calls for experimental efforts to grow high quality single phase Fe_4N and $MnFe_3N$ films in the (011) crystal directions. Under pressure and at low temperatures, dynamical instability with soft phonon modes start to appear in Fe_4N and $MnFe_3N$ at about 14 GPa and 21 GPa, respectively. But the strong phonon anharmonic interactions in these materials can lift the dynamical instability even at the room temperature, and the structures of Fe_4N and $MnFe_3N$ can remain dynamically stable up to pressures of about 30 GPa, which is consistent with high-pressure X-ray diffraction experiments. In this work, we have unveiled the simultaneous presence of several unusual mechanisms in Fe_4N and its substitution doped derivative structure $MnFe_3N$, including strong electron correlation, large nonlinear stress response, and strong lattice anharmonicity, which produce fundamentally interesting and practically useful magnetic and mechanical properties. The obtained results are expected to have important implications for optimal design of these materials in wide-ranging applications in electronic and spintronic devices.

V. ACKNOWLEDGEMENT

This work was supported by NNSF of China (No. 11174200) at SJTU and DOE (DE-NA0001982) at UNLV.

---

* Corresponding author; Email:hsun@sjtu.edu.cn

† Corresponding author; Email:chen@physics.unlv.edu

[1] K. Hussain, A. Tauqir, A. ul Haq, and A. Q. Khan, Int. J. Fatigue **21**, 163 (1999).

[2] E. A. Ochoa, C. A. Figueroa, and F. Alvarez, Surf. Coat. Tech. **200**, 2165 (2005).

[3] R. M. M. Riofano, L. C. Casteletti, L. C. F. Canale, and G. E. Totten, Wear **265**, 57 (2008).

[4] T. Nakamoto, N. Shirakawa, N. Ueda, Y. Miyata, and T. Sone, Surf. Coat. Tech. **202**, 5484 (2008).

[5] H. Jacobs, D. Rechenbach, and U. Zachwieja, J. Alloy. Compd. **227**, 10 (1995).

[6] C. L. Yang, M. M. Abd-Elmeguid, H. Micklitz, G. Michels, J. W. Otto, Y. Kong, D. S. Xue, and F. S. Li, J. Magn. Magn. Mater. **151**, L19 (1995).

[7] N. Ishimatsu, H. Maruyama, N. Kawamura, M. Suzuki, Y. Ohishi, M. Ito, S. Nasu, T. Kawakami, and O. Shimomura, J. Phys. Soc. Jpn. **72**, 2372 (2003).

[8] J. F. Adler and Q. Williams, J. Geophys. Res. **110**, B01203 (2005).

[9] A. Narahara, K. Ito, T. Suemasu, Y. K. Takahashi, A. Ranajikanth, and K. Hono, Appl. Phys. Lett. **94**, 202502 (2009).

[10] R. Niewa, D. Rau, A.Wosylus, K. Meier, M.Wessel, M. Hanfland, R. Dronskowski, and U. Schwarz, J. Alloy. Compd. **480**, 76 (2009).

[11] K. Ito, K. Okamoto, K. Harada, T. Sanai, K. Toko, S. Ueda, Y. Imai, T. Okuda, K. Miyamoto, A. Kimura, and T. Suemasu, J. Appl. Phys. **112**, 013911 (2012).

[12] K. Guo, D. Rau, J von Appen, Y. Prots, W. Schnelle, R. Dronskowski, R. Niewa, and U. Schwarz, High Pressure Res. **33**, 684 (2013).

[13] M. Ogura and H. Akai, Hyperfine Interact. **158**, 19 (2004).

[14] S. Kokado, N. Fujima, K. Harigaya, H. Shimizu, and A. Sakuma, Phys. Rev. B **73**, 172410 (2006).

[15] T. Gressmann, M. Wohlschlogel, S. Shang, U. Welzel, A. Leineweber, E. J. Mittemeijer, and Z.

K. Liu, Acta Mater. **55**, 5833 (2007).

[16] A. V. GilRebaza, J. Desimoni, and E. L. P. Blanca, Physica B **404**, 2872 (2009).

[17] J. Yang, H. Sun, and C. F. Chen, Appl. Phys. Lett. **94**, 151914 (2009).

[18] E. L. P. Blanca, J. Desimoni, N. E. Christensen, Heike Emmerich, and S. Cottenier, Phys. Status Solidi B **246**, 909 (2009).

[19] Y. Imai, Y. Takahashi, and T. Kumagai, J. Magn. Magn. Mater. **322**, 2665 (2010).

[20] Y. Takahashi, Y. Imai, and T. Kumagai, J. Magn. Magn. Mater. **323**, 2941 (2011).

[21] A. V. dos Santos, J. V. Santos, and M. A. Costa, Mater. Res. **16**, 1260 (2013).

[22] C. M. Fang, R. S. Koster, W. F. Li, and M. A. van Huis, RSC Adv. **4**, 7885 (2014).

[23] D. M. Borsa, S. Grachev, D. O. Boerma, and J. W. J. Kerssemakers, Appl. Phys. Lett. **79**, 994 (2001).

[24] R. Loloee, K. R. Nikolaev, and W. P. Pratt, Jr., Appl. Phys. Lett. **82**, 3281 (2003).

[25] J. L. Costa-Kramer, D. M. Borsa, J. M. Garcia-Martin, M. S. Martin-Gonzalez, D. O. Boerma, and F. Briones, Phys. Rev. B **69**, 144402 (2004).

[26] J. M. Gallego, S. Yu. Grachev, D. M. Borsa, D. O. Boerma, D. Ecija, and R. Miranda, Phys. Rev. B **70**, 115417 (2004).

[27] C. Navio, J. Alvarez, M. J. Capitan, D. Ecija, J. M. Gallego, F. Yndurain, and R. Miranda, Phys. Rev. B **75**, 125422 (2007).

[28] P. Mohn, K. Schwarz, S. Matar, and G. Demazeau, Phys. Rev. B **45**, 4000 (1992).

[29] C. Paduani, J. Appl. Phys. **96**, 1503 (2004).

[30] J. von Appen and R. Dronskowski, Angew. Chem. Int. Ed. **44**, 1205 (2005).

[31] D. Musica and J. M. Schneider, Appl. Phys. Lett. **88**, 031914 (2006).

[32] Z. J. Wu and J. Meng, Appl. Phys. Lett. **90**, 241901 (2007).

[33] E. J. Zhao, H. P. Xiang, J. Meng, and Z. J. Wu, Chem. Phys. Lett. **449**, 96 (2007).

[34] A. V. G. Rebaza, J. Desimoni, E. L. P. Blanca, Physica B **407**, 3240 (2012).

[35] P. Monachesi, T. Bjorkman, T. Gasche, and O. Eriksson, Phys. Rev. B **88**, 054420 (2013).

[36] J. Martinez, L. Lopardo, and J. Desimoni, J. Alloy. Compd. **557**, 218 (2013).

[37] C. Jiang and S. G. Srinivasan, *Nature* **496**, 339 (2013).

[38] P. Souvatzis, O. Eriksson, M. I. Katsnelson, and S. P. Rudin, Phys. Rev. Lett. **100** 095901 (2008).

[39] J. A. Chan, J. Z. Liu, H. Raebiger, S. Lany, and A. Zunger, Phys. Rev. B **78** 184109 (2008).

[40] T. Zhang, Z. L. Lv, Y. Cheng, X. R. Chen, and G.F. Ji, Comp. Mater. Sci. **84** 156 (2014).

[41] D. Roundy, C. R. Krenn, M. L. Cohen, and J. W. Morris Jr., Phys. Rev. Lett. **82**, 2713 (1999).

[42] R. H. Telling, C. J. Pickard, M. C. Payne, and J. E. Field, Phys. Rev. Lett. **84**, 5160 (2000).

[43] S. H. Jhi, S. G. Louie, M. L. Cohen, and J. W. Morris Jr., Phys. Rev. Lett. **87**, 075503 (2001).

[44] S. Ogata, J. Li, and S. Yip, Science **298**, 807 (2002).

[45] Y. Zhang, H. Sun, and C. F. Chen, Phys. Rev. Lett. **93**, 195504 (2004).

[46] Y. Zhang, H. Sun, and C. F. Chen, Phys. Rev. Lett. **94**, 145505 (2005).

[47] Z. C. Pan, H. Sun, and C. F. Chen, Phys. Rev. Lett. **98**, 135505 (2007).

[48] J. Yang, H. Sun, and C. F. Chen, J. Am. Chem. Soc. **130**, 7200 (2008).

[49] C. R. Krenn, D. Roundy, M. L. Cohen, D. C. Chrzan, and J. W. Morris Jr., Phys. Rev. B **65**, 134111 (2002).

[50] M. I. Eremets, I. A. Trojan, P. Gwaze, J. Huth, R. Boehler, and V. D. Blank, Appl. Phys. Lett. **87**, 141902 (2005).

[51] T. Li, J. W. Morris Jr., N. Nagasako, S. Kuramoto, and D. C. Chrzan, Phys. Rev. Lett. **98**, 105503 (2007).

[52] See the web site: http://www.vasp.at/

[53] a) P. E. Blöchl, Phys. Rev. B **50**, 17953 (1994); b) G. Kresse and J. Joubert, Phys. Rev. B **59**, 1758 (1999).

[54] J. P. Perdew, K. Burke, and M. Ernzerhof, Phys. Rev. Lett. **77**, 3865 (1996).

[55] a) M. P. Teter, M. C. Payne, and D. C. Allan, Phys. Rev. B **40**, 12255 (1989); b) D. M. Bylander, L. Kleinman, and S. Lee, Phys Rev. B **42**, 1394 (1990).

[56] H. J. Monkhorst and J. D. Pack, Phys. Rev. B **13**, 5188 (1976).

[57] See the web site: http://phonopy.sourceforge.net/

[58] See the web site: http://uquantchem.com/scaild.html